Reticular Synthesis of Flexible Rare-Earth Metal-Organic Frameworks: Control of Structural Dynamics and Sorption Properties Through Ligand Functionalization

Edward Loukopoulos,[a] Giasemi K. Angeli,[a, b] Constantinos Tsangarakis,[a] Eleni Traka,[a] Konstantinos G. Froudas,[a] and Pantelis N. Trikalitis*[a]

An exciting direction in metal-organic frameworks involves the design and synthesis of flexible structures which can reversibly adapt their structure when triggered by external stimuli. Controlling the extent and nature of response in such solids is critical in order to develop custom dynamic materials for advanced applications. Towards this, it is highly important to expand the diversity of existing flexible MOFs, generating novel materials and gain an in-depth understanding of the associated dynamic phenomena, eventually unlocking key structure-property relationships. In the present work, we successfully utilized reticular chemistry for the construction of two novel series of highly crystalline, flexible rare-earth MOFs, RE-**thc**-MOF-2 and RE-**teb**-MOF-1. Extensive single-crystal to single-crystal structural analyses coupled with detailed gas and vapor sorption studies, shed light onto the unique responsive behavior. The development of these series is related to the reported RE-**thc**-MOF-1 solids which were found to display a unique continuous breathing and gas-trapping property. The synthesis of RE-**thc**-MOF-2 and RE-**teb**-MOF-1 materials represents an important milestone as they provide important insights into the key factors that control the responsive properties of this fascinating family of flexible materials and demonstrates that it is possible to control their dynamic behavior and the associated gas and vapor sorption properties.

Introduction

The chemistry and applications of flexible metal-organic frameworks (MOFs) have been receiving an exceptional amount of attention in recent years.[1–6] These dynamic materials display unique features as they can reversibly switch their structure between an open and a closed pore phase, responding to the triggers of external stimuli (e.g., guest molecules, temperature, pressure or light). This behavior can be then exploited to generate novel materials with distinctive uses, compared to rigid frameworks, in various fields of high interest. Accordingly, responsive MOFs have been notably utilized for the controlled

adsorption,[7] trapping[8] and separation[9–11] of gases, the responsive sensing of various molecules,[12–14] the synthesis of efficient drug delivery systems[15] and as switchable catalysts with tunable activity.[16–17]

The ultimate goal in flexible MOF research is to fully understand the observed dynamic responses and precisely control them towards specific applications, eventually developing adaptive tailor-made materials with advanced properties.[18–20] In order to completely realize this potential, it is necessary to expand the diversity of existing flexible MOFs, in terms of both chemical and structural composition, generating new families of dynamic materials with varying extents of response. This will allow us to gain a deep knowledge of the relationship between the responsive structures in flexible MOFs and the external physical environment. Within this context, the choice of a suitable linker is a critical parameter[21] in order to introduce and regulate flexibility in MOFs. The most established method for this is ligand modification, in which functional groups are introduced in order to increase interaction with external stimuli such as guest molecules or light.[22–25] A recent review by Senkovska et al. details multiple examples where the change of even a single atom in the organic linker can have notable consequences in the resulting flexibility.[26] Another emerging strategy involves the use of linkers with reduced symmetry. This approach generally guides the synthesis towards less predictable MOFs with increased structural complexity and diversity,[27–30] which in turn can promote dynamic behavior.[8]

Very recently we reported[8] the synthesis of the RE-**thc**-MOF-1 series, a novel family of MOFs derived from the combination of rare earth (RE) metals with the 4-connected (4-

[a] Dr. E. Loukopoulos, Dr. G. K. Angeli, Dr. C. Tsangarakis, E. Traka,
K. G. Froudas, Prof. P. N. Trikalitis
Department of Chemistry
University of Crete
Voutes 71003 Heraklion (Greece)
E-mail: ptrikal@uoc.gr

[b] Dr. G. K. Angeli
Theoretical and Physical Chemistry Institute
National Hellenic Research Foundation
48 Vassileos Constantinou Avenue, Athens, 11635 (Greece)

Chem. Eur. J. 2024, 30, e202302709 (1 of 13)

© 2023 The Authors. Chemistry - A European Journal published by Wiley-VCH GmbH

Chemistry–A European Journal

Research Article
doi.org/10.1002/chem.202302709

Chemistry Europe
European Chemical
Societies Publishing

c) asymmetric organic linker H$_4$CPTTA (5′-(4-carboxyphenyl)-[1,1′:3′,1″-terphenyl]-3,4″,5-tricarboxylic acid), or H$_4$**L**. It is noted that flexible RE-MOFs are very rare but highly desirable as multifunctional responsive solids due to the combination of RE optical and chemical properties with framework dynamics. The RE-**thc**-MOF-1 structures are composed of RE$_6$ clusters with an asymmetric 8-c connectivity, which serve as the secondary building blocks. These MOFs exhibited significant dynamic behavior, which was largely expressed by notable changes in ligand conformation, including an evident rotation of some aromatic rings and a large hinge-like motion affecting certain coordination angles. Due to the extent of this flexibility, the materials also displayed gas trapping capabilities, in which an amount of the adsorbate remained inside the framework after desorption and could not be released at cryogenic conditions under ultrahigh vacuum.

To expand on these concepts, we explored possible strategies including reticular chemistry that would allow us to further regulate the dynamic phenomena. Linker functionalization was chosen as a feasible method, and as a result the ligands 5-(2,6-bis(4-carboxyphenyl)pyridin-4-yl)isophthalic acid (H$_4$BCPIA, or H$_4$**L$_1$**) and 5′-(4-carboxy-2-methylphenyl)-2″-methyl-[1,1′:3′,1″-terphenyl]-3,4″,5-tricarboxylic acid (H$_4$CMTTA, or H$_4$**L$_2$**) were designed and synthesized (Figure 1a, Schemes S1-S2, Figures S1–S6). Both ligands are asymmetric, tetratopic carboxylate-based linkers that are analogous to H$_4$**L**. However, in H$_4$**L$_1$** the central aromatic ring is pyridine instead of benzene, while H$_4$**L$_2$** contains a methyl group in each benzoate group. These subtle modifications can have drastic consequences in the resulting structure and dynamic phenomena: the presence of a nitrogen atom in the central aromatic ring of H$_4$**L$_1$** decreases the

steric hindrance between the central ring and the connecting benzoate groups, allowing for more unrestrained rotation of these rings. This is especially important, having in mind that the dynamic motions of the benzoate groups played a crucial role in the eventual flexibility observed in the RE-**thc**-MOF-1 series.[8] Furthermore, the nitrogen atom can potentially function as an additional binding site or as an acceptor atom for the formation of guest-framework interactions, also affecting the resulting flexibility. On the other hand, the additional methyl groups in H$_4$**L$_2$** aim to produce the opposite effect in steric hindrance, as the analogous aromatic moieties can now rotate less freely.

Following this approach, we herein report the reticular synthesis and characterization of two RE-MOF families, denoted as RE-**thc**-MOF-2 (using H$_4$**L$_1$** and Y^{3+}, Sm^{3+}, Eu^{3+}, Tb^{3+}, Dy^{3+}, Ho^{3+} or Er^{3+} as the rare earths) and RE-**teb**-MOF-1 (using H$_4$**L$_2$** and Y^{3+}, Eu^{3+} or Er^{3+}). These crystalline MOFs (Figures S7–S17) are based on differing 8-connected hexanuclear [RE$_6$(μ_3-X)$_8$(–COO)$_8$]$^{2+}$ clusters (X: OH$^-$/F$^-$), resulting in a new (3,3,8)-c **teb** topology in the case of the latter family. Both series of materials also exhibit varying degrees of extraordinary dynamic behavior, in terms of coordination and conformation, upon removal/insertion of guest molecules; these transitions were tracked by single-crystal structural analysis (Tables S1–S15). More importantly, a comparison of these families with the H$_4$**L**-based RE-**thc**-MOF-1 series reveals that the emergence of slight differences in coordination environment as well as the formation of additional host-guest interactions drastically affects the breathing capabilities and the eventual sorption properties. As a notable consequence, the RE-**teb**-MOF-1 series displays gas trapping properties with newly-observed behavior and features. These results highlight the use of ligand
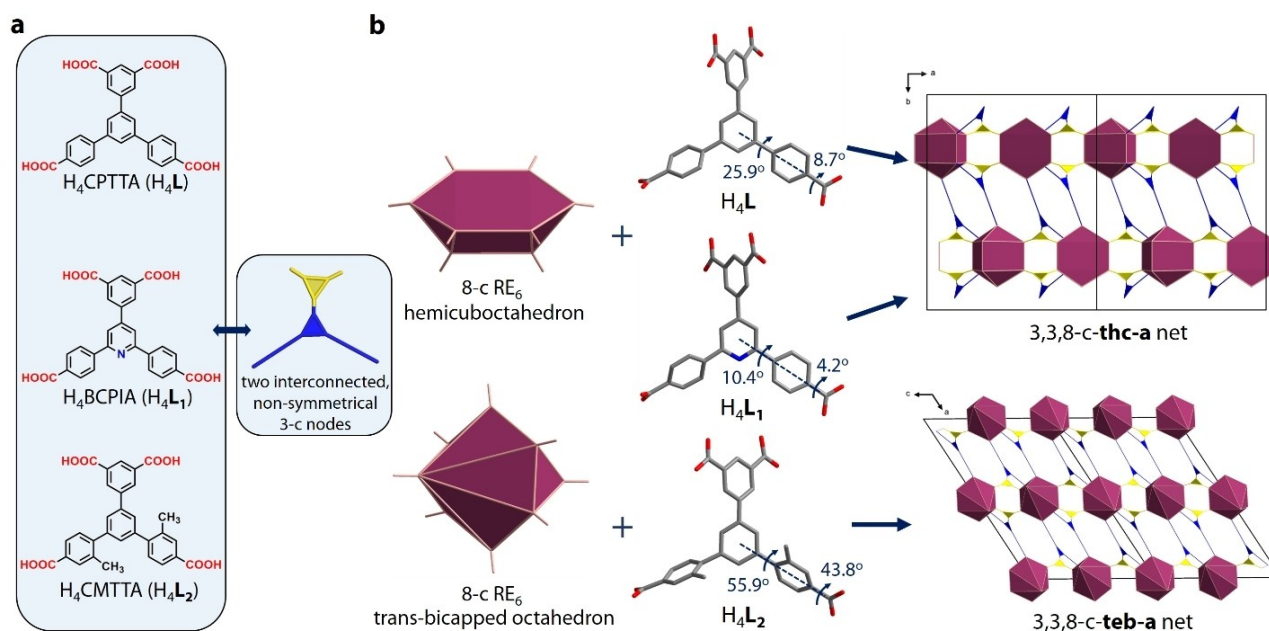

Figure 1. a) The conceptual design of tetratopic ligands H$_4$**L$_1$** and H$_4$**L$_2$** through functionalization of the initial asymmetric linker H$_4$**L**, and their geometrical representation as two interconnected non-symmetrical 3-c triangular nodes. b) The different type of ligand functionalization leads to two different types of 8-c RE$_6$ clusters, shaped either as a hemi-cuboctahedron or a trans-bicapped octahedron, resulting in the respective generation of the augmented **thc-a** and **teb-a** nets.

functionalization as a powerful strategy for the control of dynamic phenomena, providing new directions toward the rational engineering of multifunctional responsive MOFs.

Results and Discussion

The RE-**thc**-MOF-2 series was prepared by reacting the corresponding rare-earth (Y^{3+}, Sm^{3+}, Eu^{3+}, Tb^{3+}, Dy^{3+}, Ho^{3+}, Er^{3+}) nitrate with H_4L_1 in *N,N*-dimethylformamide (DMF) under solvothermal conditions and in the presence of 2-fluorobenzoic acid (2-FBA). A similar synthetic route was employed to afford representative members (Y^{3+}, Eu^{3+}, Er^{3+}) of the RE-**teb**-MOF-1 family, using the H_4L_2 linker instead. The use of 2-FBA is essential and plays a multiple role in the formation of these MOFs: (i) Its use in MOF synthesis as a coordinating modulator that enhances crystallinity have been well established in several studies.[31–34] (ii) As demonstrated recently, fluorinated modulators such as 2-FBA promote the formation of polynuclear clusters as building blocks in RE-MOFs, containing μ_3-X⁻ (X: OH⁻ or F⁻) bridging groups.[4,35–37] (iii) As seen in the RE-**thc**-MOF-1 family, 2-FBA molecules coordinate to the RE_6 cluster as non-bridging ligands, essentially co-directing the asymmetric connectivity of the cluster and the resulting topology. (iv) The presence of 2-FBA ligands in RE-**thc**-MOF-1 was also found to be crucial for its breathing behavior. As detailed in the next sections, this is also observed in varying degrees in the RE-**thc**-MOF-2 and RE-**teb**-MOF-1 series.

Structural analysis and flexibility studies of RE-thc-MOF-2

Single-crystals for all members of the RE-**thc**-MOF-2 series were afforded using the above synthetic strategy. The corresponding single-crystal X-ray diffraction (SCXRD) analysis revealed that all MOFs are isostructural (Tables S1, S3, S5–S12) and therefore only the representative structure of the Yttrium analogue will be described in detail. Accordingly, Y-**thc**-MOF-2 crystallizes in the orthorhombic *Pnma* space group, with unit cell $a = 25.8894(9)$ Å, $b = 32.8207(11)$ Å, $c = 14.8169(5)$ Å and $V = 12590.0(7)$ Å³. As in the RE-**thc**-MOF-1 series, the structure is composed of 8-connected hexanuclear clusters based on an octahedral $[Y_6(\mu_3\text{-}X)_8]$ core (Figure 2a). These serve as the inorganic building blocks and are connected by L_1^{4-} ligand molecules to generate the resulting architecture. Looking down the *ac* plane, the framework is best described as a layered structure, in which the isophthalate group of the ligand connects neighboring clusters along the *a* axis while one benzoate group acts as a pillar that links these layers, extending the framework along the *b* axis (Figures 2a-top, b and S18). There are four crystallographically independent Yttrium ions
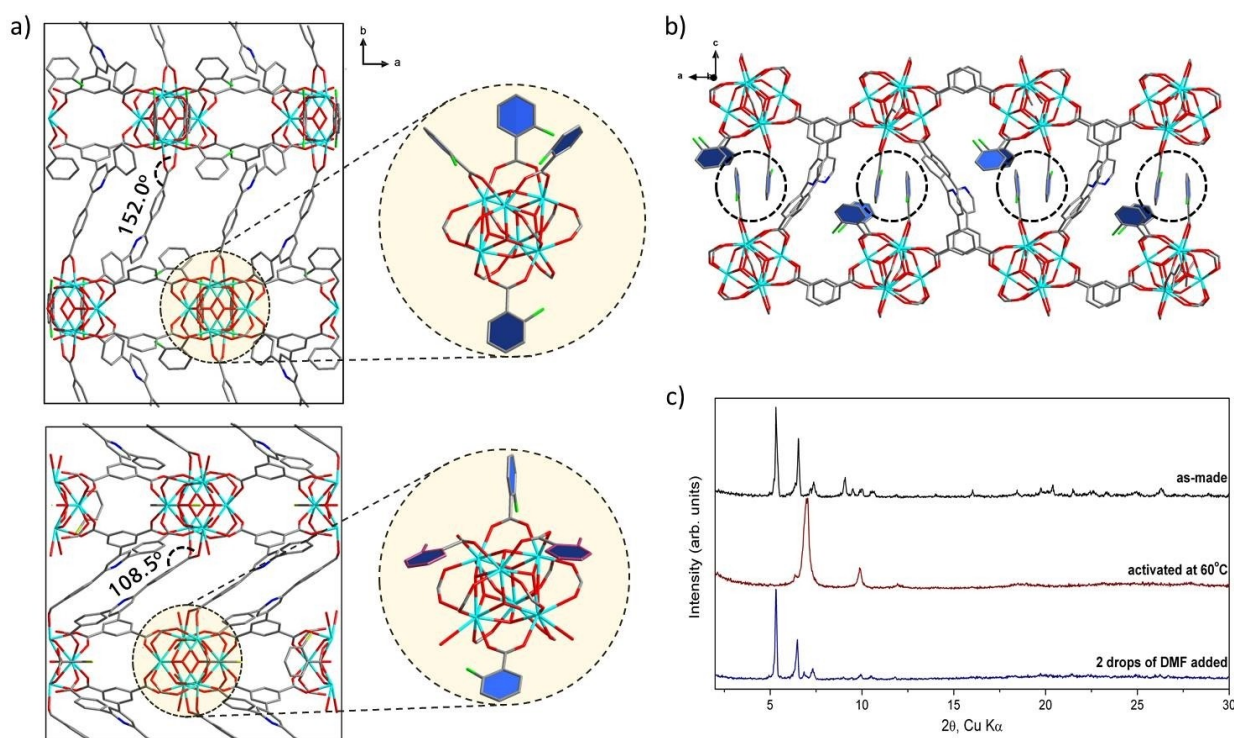

Figure 2. a) View of the unit cell of the open (top) and closed (bottom) phase of Y-**thc**-MOF-2, displaying the dynamic hinge-like motion of the layered-connecting benzoate group. The conformation of the coordinated 2-FBA ligands on the metal cluster is shown for each phase in circles, highlighting their severe deformation between the open and the closed form of the structure. b) The structure of a single layer looking down the *ac* plane, in the open phase of Y-**thc**-MOF-2. The dashed circles highlight the presence of π⋯π interactions between coordinated 2-FBA ligands in neighboring clusters. c) Experimental PXRD patterns of Y-**thc**-MOF-2 as-made in DMF (black), after activation of the EtOH-exchanged sample at 60 °C under dynamic vacuum (red) and after re-addition of a few drops of DMF (blue), indicating the presence of dynamic phenomena during insertion/removal of guest molecules.

Chemistry–A European Journal

Research Article
doi.org/10.1002/chem.202302709

Chemistry Europe
European Chemical
Societies Publishing

observed within each Y_6 cluster, displaying different coordination environment. Two of those (Y2 and Y4) are 8-coordinated and occupy the axial positions of the octahedron, while the remaining ions (Y1 and Y3) have a coordination number of 9 and are found in the equatorial positions along with symmetry related metal centers. Four 2-FBA anions are also coordinated to this cluster, bridging adjacent Yttrium ions of the same cluster. The conformation and position of these molecules is unusual, with three 2-FBA anions residing on one side of the cluster, while the fourth 2-FBA molecule is found at its opposite end (Figure 2a-top, circle). As a result of this arrangement, the former three 2-FBA create a narrow pocket of space that expands within the layers of the structure and along the c axis (Figure 2b). This pocket is filled by another 2-FBA molecule that resides in the opposite side of a neighboring Y_6 cluster and forms a strong $\pi\cdots\pi$ interaction (centroid-centroid distance of 2.813(2) Å) with one of the remaining three 2-FBA (Figures 2b and S19). The steric effects caused by this conformation increases the width of the pocket significantly compared to the one observed in RE-**thc**-MOF-1 (Figures S20-S22). Four DMF solvent molecules are also coordinated to the cluster to complete its coordination sphere. As the resulting framework is anionic, the structure fulfills the charge balance through the presence of disordered dimethylammonium cations that derive from the decomposition of DMF molecules. Considering all of the above, the complete chemical formula of Y-**thc**-MOF-2 is $[(CH_3)_2NH_2]_2[Y_6(\mu_3-X)_8(L_1)_2(2\text{-}FBA)_4(DMF)_4]$. The non-symmetric placement of the 2-FBA molecules also directs the asymmetric connectivity of the $[Y_6(\mu_3-X)_8]$ core. As seen in Figure 1(b), the 8 points of extension of the corresponding $[Y_6(\mu_3-X)_8(-COO)_8]$ inorganic node result in an 8-vertex building block of a hemi-cuboctahedron. Concurrently, the tetratopic organic ligand is best represented geometrically as two interconnected 3-c triangular nodes. As a result, the framework displays the unusual (3,3,8)-c **thc** topology.

Powder X-ray diffraction (PXRD) experiments (Cu Kα radiation) on the RE-**thc**-MOF-2 series confirmed the phase purity of the crystalline materials, as the corresponding patterns matched well with the ones simulated from the crystal structures (Figure S27). More importantly, a series of successive PXRD measurements over time revealed that the RE-**thc**-MOF-2 series, when exposed to air, undergo a continuous phase transformation as the guest solvent molecules within the pores evaporate. At the same time, these materials retain their crystallinity and exhibit excellent chemical stability. More specifically, for the representative member Er-**thc**-MOF-2, the PXRD pattern of as-made material in DMF begins to change after 1 hour of air exposure and stabilized after 3 hours. Within this period, significant differences are observed in the low angle region, as the initial major peaks at 5.29° and 6.47° 2theta gradually shift to higher 2theta angles, indicating shrinkage of the unit cell (Figure S28). This effect appears more pronounced after 18 hours of exposure, with the relevant peaks appearing at 6.59° and 6.90°, respectively. Similar flexibility effects but with much faster kinetics were observed when the material was exchanged with solvents of lower boiling points (Figures S29–S31). Notably, these phase transformations appear to be fully

reversible, as the PXRD pattern of the open phase is re-obtained upon introduction of additional solvent to the dry material (Figures 2c and S29–S32). This continuous breathing behavior is uncommon in flexible MOFs, as typically a phase transition occurs between specific and distinct crystal structures.[3]

Having established the presence of flexibility, we then took advantage of the exceptionally high stability and crystallinity in these materials (compared to most RE-MOFs with unsaturated metal sites in the literature[27]) to further explore these phenomena through additional SCXRD experiments. A suitable ethanol-exchanged crystal of Y-**thc**-MOF-2 was firstly selected from a wet sample and was then immediately mounted under nitrogen stream at 200 K. In agreement with the PXRD data, the unit cell determination for this sample showed that the framework remains similar to the as-made structure (See Table S1). The sample temperature was then slowly raised to 290 K, to ensure smooth evaporation of the guest ethanol molecules and retain the quality of the crystal. Remarkably, after 20 minutes at 290 K, a unit cell measurement revealed a significant shrinkage of the b axis by 18.48% (from 32.8207(11) to 26.755(3) Å) compared to the as-made framework. This is also accompanied by a much lower cell volume (from 12590.0(7) to 9886.3(16) Å³). At the same time, the drop in the remaining cell lengths is much smaller ($\Delta a = 0.52$ Å, $\Delta c = 0.25$ Å), while the symmetry remains unchanged. An ensuing SCXRD analysis showed that the breathing phenomena mainly derive from major changes in the conformation and coordination mode of the ligand. More specifically, a severe hinge-like motion (Figure 2a-bottom) is observed in layer-connecting benzoate groups, reducing the coordination angle between this carboxylate and the $Y_2=O_2$ plane down to 108.5° ($\Delta\theta = 43.5°$). The conformation of the 2-FBA molecules within the Y_6 cluster also changes significantly during the breathing process (Figures 2a-bottom circle and S20–S21). A closer look in the first three 2-FBA anions found on one side of the cluster, reveals that the aromatic ring in the central anion rotates heavily around the $C\cdots C_{carboxylate}$ vector, with the relevant dihedral angle measured at 92.2°. Although the two neighboring 2-FBA molecules were only partially modelled due to the quality of the diffraction data, it was possible to determine their directionality and coordination mode. Particularly, a large bending effect is observed as each 2-FBA rotates around the $O\cdots O$ vector of its carboxylate group to form an unusually low coordination angle of 113.5° with the $Y_2=O_2$ plane (Figure 2a-bottom circle). This effect is in agreement with the "Venus flytrap"-like motion seen in the analogous molecules in the RE-**thc**-MOF-1 materials (Figure S20). As in the as-made framework, the pocket created by these three 2-FBA is filled by a fourth 2-FBA molecule of a neighboring cluster. However, this molecule now also shows a slight bend to accommodate for the conformation changes within the pocket. This eventually translates to a lower coordination angle by 12.7°, reaching a value of 152.3° (Figures S20–S21).

Structural analysis and flexibility studies of RE-teb-MOF-1

As a representative member of the RE-**teb**-MOF-1 materials, the as-made Y-**teb**-MOF-1 crystallizes in the monoclinic C2/c space group and displays the unit cell $a = 38.723(2)$ Å, $b = 14.3624(8)$ Å, $c = 25.4610(15)$ Å, $\beta = 122.961(3)°$ and $V = 11881.1(12)$ Å^3. Once again, the inorganic building blocks in the framework are hexanuclear Yttrium clusters that display 8-c connectivity, linked together by L_2^{4-} organic ligands (Figure 3a). Similarly to the RE-**thc**-MOF-2 series described earlier, four 2-FBA and DMF molecules are also coordinated to the cluster. This leads to an anionic framework and the material has a complete chemical formula of $[(CH_3)_2NH_2]_2[Y_6(\mu_3-X)_8(L_2)_2(2\text{-}FBA)_4(DMF)_4]$. However, there are considerable differences in RE-**teb**-MOF-1 compared to the RE-**thc**-MOF-2 structures. In particular, the methyl groups in H_4L_2 increase the steric hindrance between the central aromatic ring and the benzoic rings, forcing them to rotate further. This is particularly evident in one of the benzoates, affecting the corresponding torsion angle which is measured at 55.9° (Figure 1b). Crucially, it also determines the directionality of the relevant $-COO^-$ group which rotates by 43.8° (Figure 1b). These values are in stark contrast to the analogous moiety in Y-**thc**-MOF-2, in which the benzoic ring and the $-COO^-$ group appear almost parallel to the central ring (corresponding torsion angles of 10.4° and 4.2°,

respectively) due to the lower steric hindrance. Both MOF series display a similar layered structure with one benzoate group of the ligand linking neighboring clusters, however the corresponding benzoate species is different in each material (Figure S14). This affects the resulting architecture, and in RE-**teb**-MOF-2 the layers extend along the ab plane, while the isophthalate group of L_2 connects clusters within the layers along the c axis (compare Figures 3c and 2b). The location of the four 2-FBA ligands also changes as each molecule is now found to a different side of the inorganic cluster (Figure S26). As a result of the above arrangements the asymmetric connectivity of the cluster is also very different and the resulting building block displays the shape of a trans-bicapped octahedron (Figure 1b). From a topological point of view, the combination of the above nodes leads to an unprecedented (3,3,8)-c net, denoted as **teb**-a.

PXRD measurements for the as-made RE-**teb**-MOF-1 also confirmed their phase purity and crystallinity, as seen in Figure S34. Successive measurements over time for the Yttrium analogue (Figure 3d) revealed that the framework displays high chemical stability under exposure to air. In addition, notable shifts (ranging from 0.1° to 0.35°) are observed throughout the pattern comparison for the (200) and (002) Bragg peaks, suggesting the occurrence of dynamic phenomena and the transition to a more contracted framework. The effect was once again attributed to the evaporation of solvent guest molecules (within the pores) from the material, and is faster in the case of
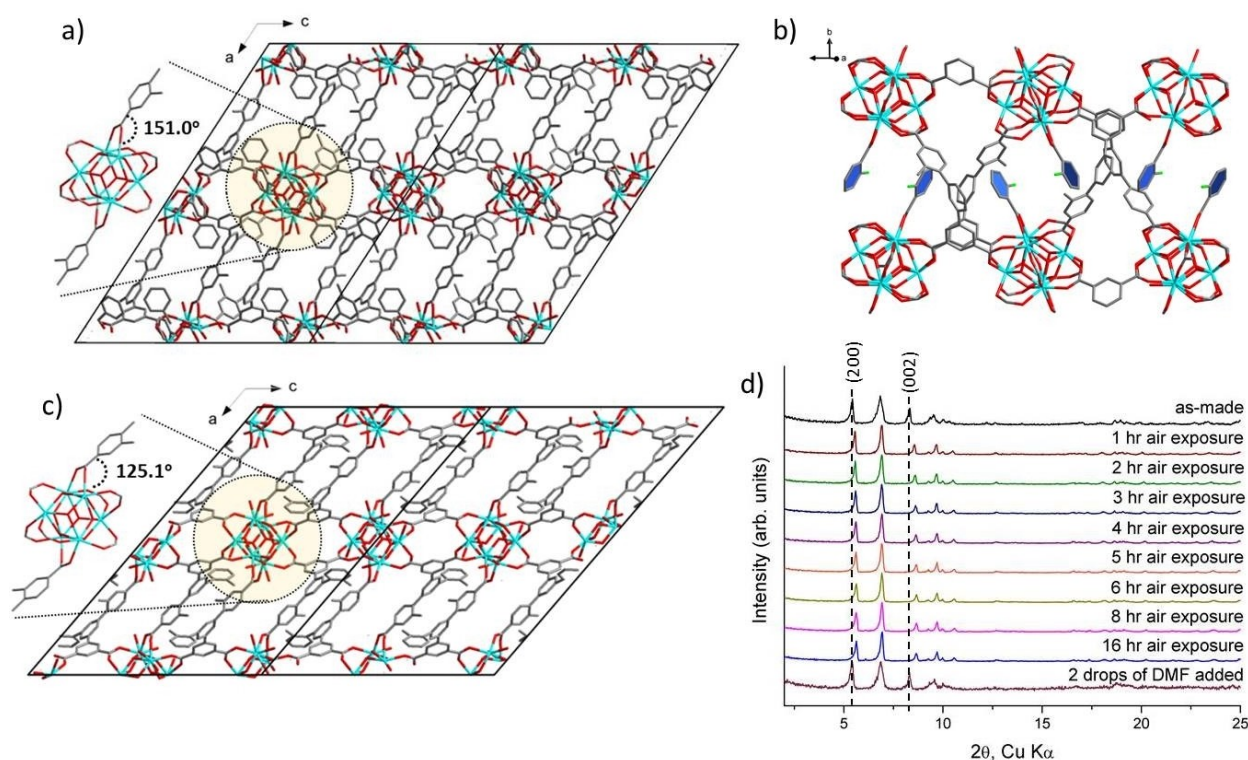

Figure 3. a) The unit cell of the as-made, open form of Y-**teb**-MOF-1, looking down the b-axis. The circle highlights the dihedral angle of the layer-connecting benzoate group that shows a dynamic hinge-like motion (coordinated 2-FBA moieties are omitted for clarity). b) The structure of the layer looking highlighting the 2-FBA ligands. c) The unit cell of the closed Y-**teb**-MOF-1 in an EtOH exchanged crystal (2-FBA are omitted for clarity). d) Experimental PXRD patterns of as-made Y-**teb**-MOF-1 over time and after adding DMF solvent, indicating the presence of dynamic phenomena during insertion/removal of guest molecules.

Chemistry–A European Journal

Research Article
doi.org/10.1002/chem.202302709

Chemistry
Europe
European Chemical
Societies Publishing

guest-exchanged materials with more volatile solvents. As seen in Figures 3(d) and S35–S37, this phenomenon is fully reversible as the framework returns to the open phase upon addition of solvent molecules.

We further evaluated this flexibility through similar temperature-dependent SCXRD investigations in an ethanol-exchanged single crystal of Y-**teb**-MOF-1 (see the SI for more details). These measurements revealed a notable increase in the β angle of the unit cell, accompanied by slight fluctuations in the a and b axis lengths. A successful dataset for the crystal was collected at 200 K after 1 hour of exposure under nitrogen stream at 280 K in order to remove excess ethanol molecules. At this point, the β angle has increased by 7.7° compared to the as-made material, leading to a narrower framework with 9.4% reduced unit cell volume ($\Delta V = 1111$ Å^3). This dynamic effect is mainly due to a hinge-like motion of the layer-connecting methylated benzoate groups, as the coordination angle between the carboxylate moiety and the $Y_2=O_2$ plane is reduced from 151.0 to 125.1° (Figure 3a). This flexibility is similar to the one seen in RE-**thc**-MOF-x (x: 1, 2) materials, although less pronounced. Furthermore, a smaller hinge-like motion (corresponding $\Delta\theta = 12.8$°) that also contributes to this flexibility is observed in the isophthalate group of L_2 that links the layers formed within the architecture of the structure. As the framework shrinks, the 2-FBA molecules also change their conformation, bending towards lower coordination angles ($\Delta\theta = 19.2$°) (Figure S26).

Gas sorption studies

A detailed gas-sorption study using different gases at their boiling point was executed in order to probe the dynamic phenomena in Y-**thc**-MOF-2 and Y-**teb**-MOF-1 and in addition, to gain important insights into the effect of the functional groups of the linkers (N-containing H_4L_1 and methyl groups on H_4L_2), as compared to the reported Y-**thc**-MOF-1 based on the pristine, non-functionalized linker H_4L.

We initiated our investigations on the gas-sorption study of Y-**thc**-MOF-2 based on protocols established for RE-**thc**-MOF-1 series, since both families displayed similar structural features and solvent stability. Initially, N_2 sorption isotherms of the Y-**thc**-MOF-2 analogue were recorded at 77 K using an ethanol exchanged sample that was activated at various temperatures (25, 40, 60 and 80 °C) under high vacuum (Figure S40). When activated at room temperature, the framework shows almost zero nitrogen uptake. Subsequent measurements were then performed in which the activation temperature was increased at 40 and 60 °C, respectively. In these isotherms, a gradual increase in uptake is observed, starting at 0.51 p/p_0. The adsorbed volume of nitrogen reaches 72.30 (40 °C) and 85.07 (60 °C) cm^3 g^{-1} at 0.99 p/p_0. The latter value corresponds to a total pore volume of 0.13 cm^3 g^{-1}. For comparison purposes, the calculated pore volumes for the open and the closed structure were also determined using the corresponding SCXRD data. These were determined to be 0.38 and 0.23 cm^3 g^{-1}, respectively, however these values are overestimated because of the

presence in the crystal structure of chemical species that cannot be modeled crystallographically (e.g., dimethylammonium cations acting as counterions and parts of 2-FBA molecules) due to their disordered nature. Finally, no adsorption was observed when the sample was activated at 80 °C. This result is consistent with our initial findings in Y-**thc**-MOF-1, in which the presence of remaining solvent molecules in the framework influences the breathing phenomena.[8] Therefore, in temperatures beyond the solvent boiling point the structure is too contracted to allow adsorption of N_2.

Considering the above, the results indicate that N_2 adsorption at 77 K up to 1 bar does not trigger a transition to a more open structure. Subsequent measurements were then made to record Ar and CH_4 sorption isotherms of Y-**thc**-MOF-2 (activated at 60 °C) at 87 and 112 K, respectively. However, no sorption isotherms were recorded due to the observed extremely slow adsorption kinetics. For example using Ar at 87 K, for the first requested point at relative pressure 1×10^{-6} p/p_0 (microporous analysis) equilibrium after dosing was not reached even after several hours. This behavior is in stark contrast to the performance of Y-**thc**-MOF-1, in which the analogous sorption of N_2, Ar and CH_4 gases at cryogenic conditions was sufficient to fully open the framework, demonstrating that one atom change in the organic linker (a nitrogen atom in H_4L_1, for a carbon atom in H_4L, see Figure 1) can have a remarkable effect on the sorption behavior in these unique materials.

In contrast, a CO_2 sorption isotherm at 195 K was successfully recorded for Y-**thc**-MOF-2 (Figure S41). In this case, a gradual increase in uptake is observed with increasing relative pressure, without any noticeable or pronounced steps. The CO_2 uptake at 0.99 p/p_0 is 146.48 cm^3 g^{-1}, corresponding to a more open framework, compared to N_2 sorption at 77 K, with a pore volume of 0.23 cm^3 g^{-1} and attributed to the polar nature of CO_2 resulting in enhanced gas-framework interactions. However, the observed pore volume corresponds to that of the closed form of Y-**thc**-MOF-2. The gas-sorption results clearly indicate that in the case of N_2, Ar, CH_4 and CO_2 at cryogenic conditions, the associated gas-framework interactions during the adsorption process provide insufficient energy to the Y-**thc**-MOF-2 framework to trigger a transition from an initial closed form to a fully open structure. This is in marked contrast to the behavior of Y-**thc**-MOF-1 and is attributed to the N-containing linker in Y-**thc**-MOF-2 which alters the flexibility of the benzoate group in terms of rotation. In particular, comparing the crystallographic data for the closed Y-**thc**-MOF-1 (taken at 280 K) and the closed Y-**thc**-MOF-2 (taken at 290 K), both benzoate groups are more co-planar in the latter case, as expected due to the pyridine-like central ring. Accordingly, the torsion angles are 15.6°/45.0° and 4.6°/30.8° in the closed form of Y-**thc**-MOF-1 and Y-**thc**-MOF-2, respectively (Figure S23). The smaller torsion angles in Y-**thc**-MOF-2 between adjacent aromatic rings are associated with an increased conjugation between them, making their relative rotation energetically more demanding. Apparently, the adsorption energy offered by N_2, Ar, CH_4 and CO_2 at their respective cryogenic conditions is not sufficient to break the conjugation between the central pyridine-like ring and adjacent benzoate groups in the linker of

the closed form of Y-**thc**-MOF-2. Remarkably, as we explain below, vapor sorption at ambient conditions is capable to open the structure.

In contrast to Y-**thc**-MOF-2, the structure of Y-**teb**-MOF-1 based on the methylated ligand reveals its full breathing properties upon gas sorption at cryogenic conditions. Although this behavior resembles that of the non-functionalized analogue, Y-**thc**-MOF-1, the observed dynamic characteristics are significantly different. Accordingly, the Ar isotherm at 87 K reveals no adsorption up to 0.15 p/p_0 where a very sharp increase in uptake is observed reaching 237 cm^3 g^{-1} at saturation (0.99 p/p_0), corresponding to a total pore volume of 0.31 cm^3 g^{-1} (Figure 4a). The latter is very close to the calculated value (0.32 cm^3 g^{-1}) from the single crystal structure of Y-**teb**-MOF-1, indicating the formation of a completely open phase. Notably, the desorption process is highly hysteretic where a large amount (53.4%) remains adsorbed down to 1×10^{-3} p/p_0. At this point a sharp decrease in the adsorbed amount occurs however, desorption and adsorption curves do not coincide even at a relative pressure of 1×10^{-4} p/p_0, where the remaining adsorbed volume corresponds to 15.8% of the total pore volume. These results suggest that the remaining amount at this very low partial pressure is in fact trapped inside the pore

space of Y-**teb**-MOF-1. To verify this, we executed a back-to-back adsorption measurement at 87 K without allowing the sample to warm up. It is noted that during the initialization of this 2nd run, the instrument applies ultra-high vacuum ($<1\times10^{-6}$ mbar) to the sample using a turbomolecular pump. The recorded isotherm show a very similar sharp increase in uptake during adsorption at 8×10^{-2} p/p_0 and also a highly hysteretic desorption process, however this time both adsorption and desorption curves coincide at low partial pressures, indicating that no adsorbed gas remains in the structure (Figure 4b). Notably, the adsorbed amount during the 2nd run at saturation (0.99 p/p_0) is equal to the corresponding adsorbed amount of the 1st run subtracting the trapped amount. This is evident in the overlay of the two back-to-back measurements where the 2nd isotherm is shifted up by the trapped amount of the 1st run (Figure 4b).

To the best our knowledge, this unique gas-trapping phenomenon has been observed only in the case of Y-**thc**-MOF-1 published recently by our group,[8] however significant differences are observed in the case of Y-**teb**-MOF-1. Although the frameworks are not directly comparable, a contrast between their gas-trapping performance provides useful information towards the involved energetics and the varying levels of
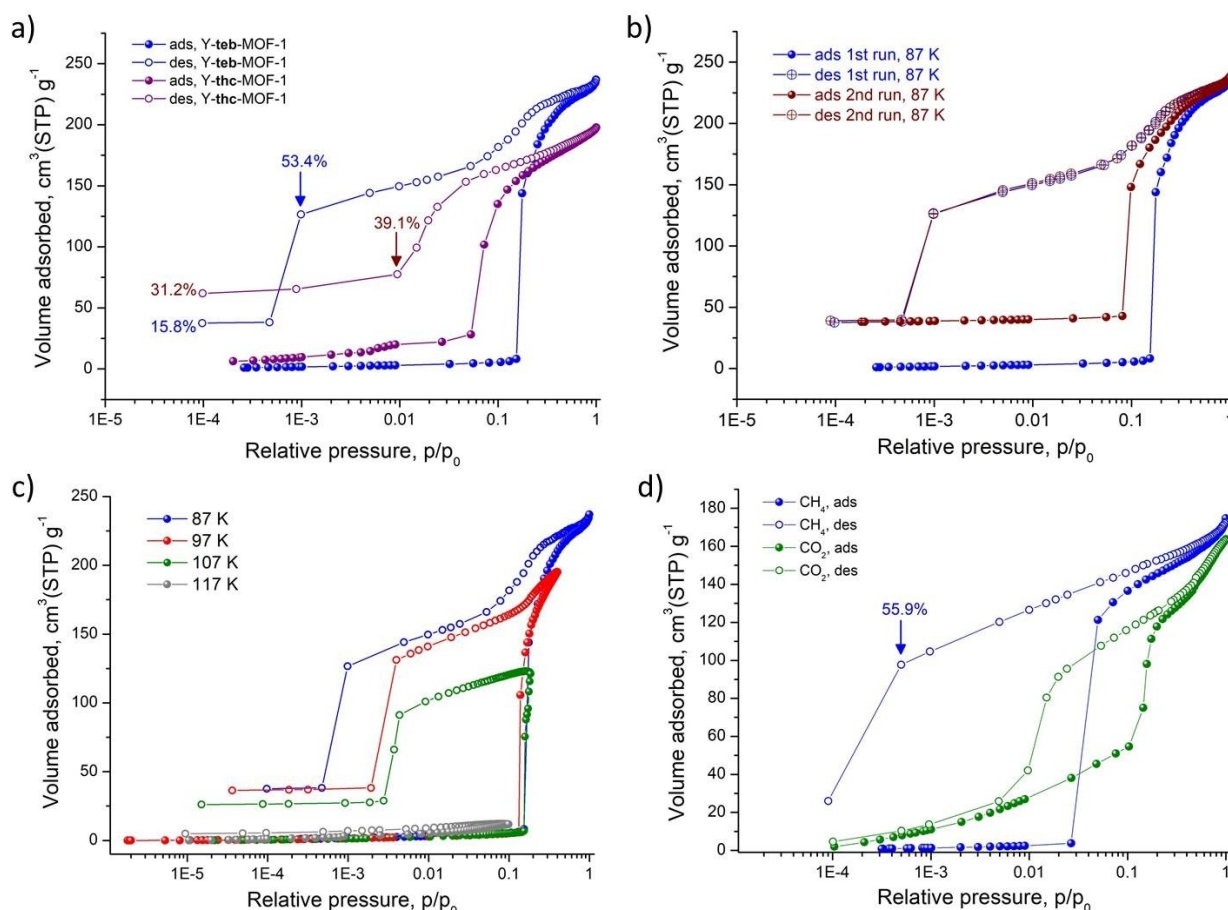

Figure 4. a) Argon sorption isotherm of Y-**teb**-MOF-1 and Y-**thc**-MOF-1, recorded at 87 K. b) Back-to-back Ar sorption measurements at 87 K of Y-**teb**-MOF-1 without an intermediate warm-up step. The second isotherm (red) is shifted up by the amount trapped from the first measurement (blue). c) Variable temperature Ar sorption isotherms of Y-**teb**-MOF-1 recorded in the range 87–117 K. d) CH$_4$ and CO$_2$ sorption isotherms of Y-**teb**-MOF-1 recorded at 112 K and 195 K respectively.

response. In particular, as shown in Figure 4(a), in the corresponding Ar sorption isotherms at 87 K, the onset of the transition in Y-**teb**-MOF-1 is shifted to a higher value of relative pressure (1.5×10^{-1} vs. 5×10^{-2} p/p_0) indicating higher energetics in this case. In other words, the framework is more difficult to open compared to Y-**thc**-MOF-1. Comparing the desorption curves, a significantly larger hysteresis loop is observed for Y-**teb**-MOF-1, where a large amount of adsorbed gas (53.4%) remains in the structure at a very low relative pressure (1×10^{-3} p/p_0), which is an order of magnitude lower compared to that of Y-**thc**-MOF-1 (1×10^{-2} p/p_0) showing also a much lower trapped amount (39.1%), see Figure 4(a). These results suggest that the adsorbed gas molecules experience a greater difficulty to escape the pore space in Y-**teb**-MOF-1, which is attributed to the more complex and sterically hindered porosity, as compare to Y-**thc**-MOF-1, originating mainly from the presence of methyl groups on the organic linkers as well as from the additional 2-FBA ligands (Y-**thc**-MOF-1 has three 2-FBA while Y-**teb**-MOF-1 has four) coordinated to the Y_6-cluster. The final trapped amount at relative pressure 1×10^{-4} p/p_0 is smaller in Y-**teb**-MOF-1 (15.8%) as compared to Y-**thc**-MOF-1 (31.2%) due to the reduced available pore volume in the former associated with the presence of the methyl-groups and also the additional 2-FBA ligands on the Y_6-cluster.

Variable temperature (VT) Ar sorption isotherms provide further insights into the flexible nature and gas-trapping properties of Y-**teb**-MOF-1 and in addition, demonstrate its distinct behavior as compared to Y-**thc**-MOF-1 for which similar experiments have been executed and published by our group.[8] In particular, with increasing temperature the relative pressure that marks the onset of framework breathing in Y-**teb**-MOF-1 remains unaltered at 1.5×10^{-1} p/p_0, however gas-trapping occurs at higher relative pressures, suggesting that the framework can close and trap gas molecules more easily. This behavior is associated with a rare continuous breathing behavior as has been explained before in Y-**thc**-MOF-1. Accordingly, a different stage of a partially open framework is reached at a given temperature and 1 bar, where the higher the temperature is, the lower is the adsorbed amount and the framework is therefore easier to close. The VT Ar sorption data show that up 107 K and 1 bar the framework of Y-**teb**-MOF-1 is still capable of breathing and trapping gas. Notably, at 117 K no Ar sorption is observed, while Y-**thc**-MOF-1 still shows its flexible nature at these conditions.[8] These results are consistent with the picture already drawn that Y-**teb**-MOF-1 is more difficult to open as compared to Y-**thc**-MOF-1.

The CH_4 sorption isotherm recorded at its boiling point (112 K) is fully consistent with the Ar sorption results (Figure 4d). Interestingly, the onset that marks the transition to the open phase is shifted to lower relative pressures at 2.7×10^{-2} p/p_0 as compared to Ar at 87 K (0.15 p/p_0), indicating favorable CH_4-framework interactions. Notably, the percent of the adsorbed CH_4 that remains trapped during desorption, at the knee that marks the transition to the closed phase (5×10^{-4} p/p_0), is 55.9%, which is very close to the corresponding value obtain using Ar at 87 K (53.9% at 1×10^{-3} p/p_0), indicating very similar responsive properties in these cases. In contrast,

although the CO_2 sorption isotherm at 195 K shows a clear transition to the open phase at a very similar relative pressure (0.1 p/p_0), a gradual CO_2 adsorption is observed until this point and also important, the desorption curve indicates that no gas is trapped, as both adsorption and desorption curves almost coincides at low relative pressures (Figure 4d). This very different behavior is attributed to the polar nature of CO_2 as well as its smaller kinetic diameter (3.3 Å) as compared to Ar (3.4 Å) and CH_4 (3.8 Å), resulting in a more facile adsorption. Interestingly, the observed highly hysteretic CO_2 isotherm of Y-**teb**-MOF-1 is in contrast to the corresponding curve obtained for Y-**thc**-MOF-1, where the hysteresis loop is significantly reduced and also the transition step is rather smaller (Figure S42). This behavior is fully consistent with the Ar sorption results, indicating that the flexible dynamics of Y-**teb**-MOF-1 are associated with higher energetics as compared with Y-**thc**-MOF-1.

Vapor sorption studies

To further probe the flexible behavior of Y-**thc**-MOF-2, we then performed a series of detailed vapor sorption measurements. For these purposes, selected vapors (water, ethanol, benzene, n-hexane) with differences in polarity, size and potential formation of host-guest interactions were chosen. The corresponding sorption isotherms recorded at 298 K up to saturation pressure are shown in Figures 5, S45 and S43. For water, the adsorption curve reveals a type III isotherm, as the adsorbed volume gradually increases up to ~0.2 p/p_0, after which a more pronounced uptake is observed (Figure S43). Nevertheless, the total uptake at saturation pressure (239.8 $cm^3 g^{-1}$) corresponds to a total pore volume of 0.19 $cm^3 g^{-1}$. This value matches well to the calculated pore volume of the closed phase, indicating the hydrophobic nature of the framework and energetically limited H_2O-framework interactions that apparently are not sufficient to trigger a transition to the open phase. The hydrophobic nature of Y-**thc**-MOF-2 is confirmed by sorption measurements of non-polar solvents, as we describe below.

In the case of ethanol, adsorption begins at low relative pressure (region of 3×10^{-4} p/p_0), thereafter increasing in an almost linear fashion up to 0.32 p/p_0 where a well-defined step is observed (Figures 5 and S45). The corresponding pore volume at this relative pressure is 0.18 $cm^3 g^{-1}$, in agreement with the closed pore phase. After the inflection point, a steep increase in uptake is observed, eventually reaching 128.45 $cm^3 g^{-1}$ at 0.99 p/p_0. The corresponding pore volume is 0.33 $cm^3 g^{-1}$ and matches the corresponding value calculated from the crystal structure of the open phase, clearly demonstrating the presence of favorable EtOH-framework interactions that provide the necessary energy to trigger the phase transition. Notably, EtOH sorption reveals the difference in the flexible behavior between Y-**thc**-MOF-2 and Y-**thc**-MOF-1 where in the latter case, the framework opens more gradual with a transition step observed at a much higher relative pressure (0.8 p/p_0), while the total uptake (101.98 $cm^3 g^{-1}$) and pore volume (0.27 $cm^3 g^{-1}$) at saturation pressure are much lower
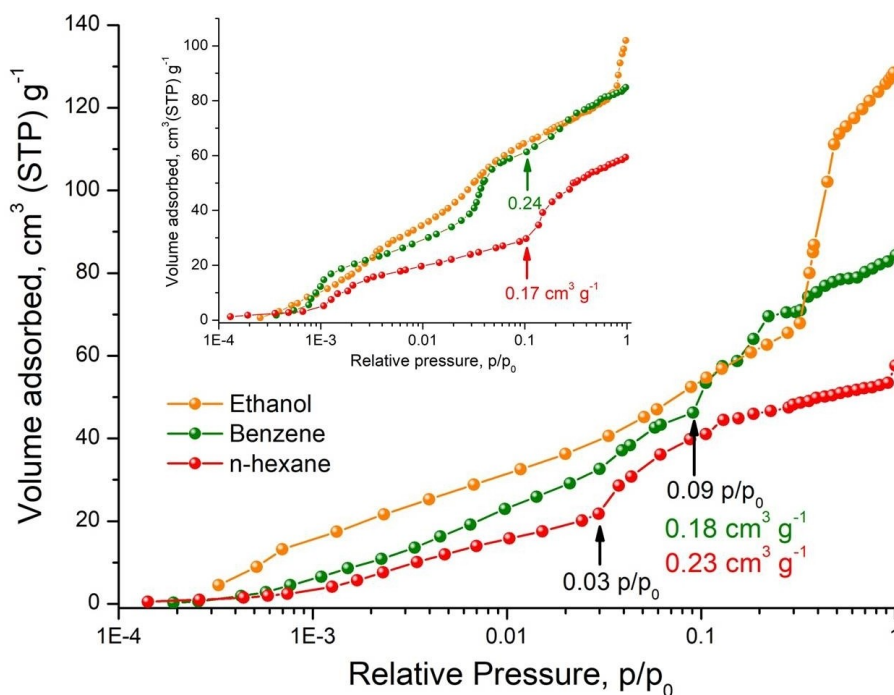
Figure 5. Vapor adsorption isotherms of Y-**thc**-MOF-2, recorded at 298 K up to saturation pressure. Inset shows the corresponding reported isotherms of Y-**thc**-MOF-1, for comparison. Desorption branches are omitted for clarity.

(Figure 5, inset). These findings clearly indicate a higher EtOH affinity for Y-**thc**-MOF-2 which is attributed to the presence of the nitrogen atom in the central ring of the linker, as revealed by crystallographic analysis. In particular, SCXRD data of the isostructural Y-**thc**-MOF-1 analogue shows the presence of EtOH molecules at the interlayer space of the framework, within a distance of ~2.8 Å from the H atom of the central aromatic ring in the organic ligand (Figure S24). The associated intermolecular interactions are therefore much stronger in the case of Y-**thc**-MOF-2 (–N–H···O due to the pyridine central ring) compared to Y-**thc**-MOF-1 (–C–H···O, benzoate ring), leading in this case to energetically enhanced EtOH-framework interactions.

The corresponding isotherms for benzene and *n*-hexane show a gradual increase in uptake associated with adsorption in the closed form of the framework up to ~0.03 p/p_0 where a step is observed indicating a transition to the open pore structure, which is more pronounced for n-hexane (Figure 5). A second distinct step is observed for benzene at ~0.09 p/p_0. At this point the amount adsorbed corresponds to a pore volume of 0.18 and 0.23 $cm^3 g^{-1}$ for benzene and *n*-hexane, respectively, indicating a more open state for the Y-**thc**-MOF-2 framework in the latter case. These results suggest a higher affinity of Y-**thc**-MOF-2 towards *n*-hexane. At saturation pressure (0.99 p/p_0) the experimental total pore volume for both vapors is 0.34 $cm^3 g^{-1}$ which matches the calculated pore volume of the open phase, indicating a complete phase transition. Remarkably, the higher affinity for *n*-hexane over benzene in Y-**thc**-MOF-2 contrasts to that in Y-**thc**-MOF-1 where a reverse affinity is observed. As shown in inset of Figure 5, Y-**thc**-MOF-1 shows a preferable adsorption for benzene over *n*-hexane as the former triggers

the framework to open at lower relative pressures and at a given p/p_0 the amount adsorbed for benzene is associated with a higher pore volume. For example, at 0.1 p/p_0 benzene sorption corresponds to a pore volume of 0.24 $cm^3 g^{-1}$ while for n-hexane is 0.17 $cm^3 g^{-1}$. Notably, these values are the opposite of those observed for Y-**thc**-MOF-2 (0.18/0.23 $cm^3 g^{-1}$ for benzene/*n*-hexane), at almost the same relative pressure, as discussed above. This reverse behavior is more difficult to be realized. Looking carefully at the isotherms, both benzene and *n*-hexane shows a well-defined adsorption step at low relative pressures (< 0.01 p/p_0) in Y-**thc**-MOF-1, where in Y-**thc**-MOF-2 a gradual and a reduced uptake is observed (the corresponding adsorption curves for Y-**thc**-MOF-2 are below that of Y-**thc**-MOF-1), indicating that in the latter case, the transition to the open phase is energetically more demanding, consistent with the gas-sorption data discussed above. However, at 0.03 p/p_0 the *n*-hexane isotherm for Y-**thc**-MOF-2 shows a clear step associated with a transition to the open phase, while for Y-**thc**-MOF-1 this is delayed and appears at 0.1 p/p_0. This behavior may reflect the differences in the pore environment between the two materials, originating from the presence of an additional coordinated 2-FBA ligand on the Y_6-clusters, in the case of Y-**thc**-MOF-2. Accordingly, *n*-hexane due to its flexible nature, could maximize the anticipated non-specific van der Waals interactions with Y-**thc**-MOF-2 framework, resulting in an increase in adsorption, as has been reported for some MOFs showing selective adsorption of *n*-hexane over benzene.[4,38–39] As we describe below, the coordinated 2-FBA ligands play a crucial role in the breathing behavior of Y-**thc**-MOF-2.

The vapor sorption isotherms recorded for Y-**teb**-MOF-1 reveal a very different flexible behavior, as compared to Y-**thc**-

Chemistry–A European Journal

Research Article
doi.org/10.1002/chem.202302709

Chemistry Europe
European Chemical
Societies Publishing

MOF-x (x: 1, 2). Due to the very interesting dynamic behavior of this material, in addition to EtOH, benzene and *n*-hexane, we recorded also water, acetonitrile and cyclohexane adsorption in order to obtain a more complete picture of its flexible properties. (Figures 6 and S46). Remarkably, except water, all organic vapors show a well-defined adsorption step associated with a transition from the closed to open pore phase, occurring however at different relative pressures, in response to particular vapor-framework interactions. Notably, EtOH triggers phase transition at the lowest relative pressure, compared to the other organic vapors, at 1×10^{-3} p/p_0, followed by *n*-hexane (4.5×10^{-3} p/p_0), CH$_3$CN (6×10^{-3} p/p_0), benzene (7×10^{-3} p/p_0) and cyclohexane (1×10^{-2} p/p_0). At saturation pressure, the obtained experimental pore volumes are very close to that calculated for the open Y-**teb**-MOF-1 (0.27, 0.28, 0.24, 0.29 and 0.24 cm^3 g^{-1} for EtOH, CH$_3$CN, *n*-hexane, benzene and cyclohexane, respectively). With the exception of *n*-hexane, the observed relative pressure onset of the transition shows a reversible relation with the polarity of the organic vapor, that is, the higher the polarity, the lower the relative pressure onset. However, the corresponding water adsorption isotherm revealed that Y-**teb**-MOF-1 is in fact hydrophobic, showing a gradual low uptake, reaching 0.1 cm^3 g^{-1}, which is well below to the expected pore volume of open Y-**teb**-MOF-1 (Figure 6). The hydrophobic nature of Y-**teb**-MOF-1 is strongly supported due to the presence of methyl group on the organic bridging ligand, L_2^{4-}. Therefore, the observed trend in vapor sorption is more complex and could involve factors such as the kinetic diameter of the vapor molecule coupled with non-specific Van der Waals interactions. Notably, the higher affinity (lower onset relative pressure) for *n*-hexane, followed by benzene and cyclohexane resembles the trend observed in the case of the recently published by our group, microporous and hydrophobic Y-**frt**-MOF-1.[4]

In comparison to the vapor sorption properties of Y-**thc**-MOF-x (x: 1, 2), significant differences are observed (Figure 5 and 6). In particular, for EtOH, the low relative pressure gradual adsorption in Y-**thc**-MOF-x (x: 1, 2) followed by a step at higher p/p_0, is now reversed in Y-**teb**-MOF-1 where a sharp step is
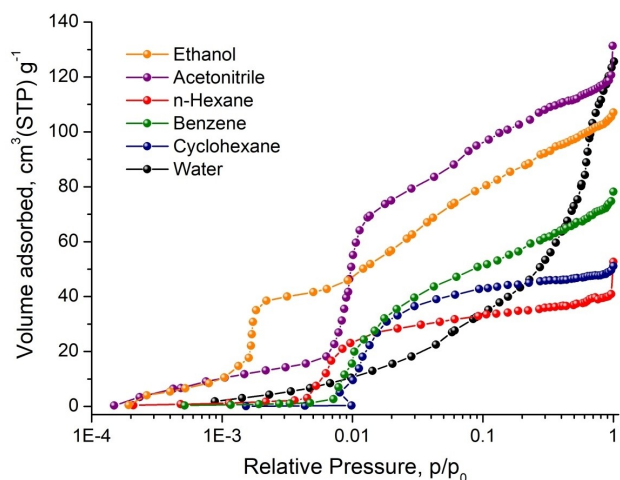
observed at 1×10^{-3} p/p_0 followed by gradual, almost linear increase in uptake up to saturation. For *n*-hexane and benzene, it is quite interesting that no adsorption occurs before the framework is triggered to open, which contrasts the gradual adsorption observed for Y-**thc**-MOF-x (x: 1, 2) even before the onset pressure. Also, for these vapors, the onset pressure appears at lower values (4.5×10^{-3} and 7×10^{-3} p/p_0 for *n*-hexane and benzene, respectively), compared to the main transition step for Y-**thc**-MOF-x (x: 1, 2). The picture that is drawn is that Y-**teb**-MOF-1 shows a higher affinity towards organic vapors, as compared to Y-**thc**-MOF-x (x: 1, 2), displaying more sharp and well-defined structural transitions which contrast to the more complex vapor sorption isotherms of the latter. As has been described in the structural analysis section (Figure 2b, 3b and S25), the layers in Y-**teb**-MOF-1 display a more complex connectivity as compared to Y-**thc**-MOF-x (x: 1, 2) and in combination with the methyl groups on the bridging ligand results in a more restrict pore space that apparently is less accessible in the closed form, which is the case at the low pressure region. Therefore, for a given vapor, there is a specific relative pressure at which the adsorption energy is sufficient for the framework to open, resulting in a sharp uptake, resulting in a more or less S-type isotherm[40] for Y-**teb**-MOF-1 (Figure 6).

Effect of coordinated 2-FBA ligands on the framework flexibility

As we have described above, in the closed form of these structures there is a considerable deformation of the bridging ligand but most importantly on the coordinated 2-FBA ligands (Figures 2, S20, S21, S26). This apparently increased energetic stage of these molecules contributes to the observed structural dynamics, as we have confirmed in the case of Y-**thc**-MOF-1.[8]

To evaluate the effect of the 2-FBA ligands in the dynamic behavior of Y-**thc**-MOF-2 and Y-**teb**-MOF-1, a post synthetic exchange was performed in both series, replacing 2-FBA with formate and hydroxo anions (see the SI for more details). The corresponding materials are denoted as Y-**thc**-MOF-2-f and Y-**teb**-MOF-1-f. Successful post-synthetic modification was confirmed by SCXRD, PXRD and NMR (^{1}H and ^{19}F) measurements (Tables S1–2, S5 and S14, Figures S33, S38, S39, S59, S60, S64, S69 and S73) demonstrating that the frameworks remain intact and also probing their flexible behavior. Importantly, the sorption properties of these materials are notably different compared to their 2-FBA containing analogues, as described below.

Following the same activation method as in the pristine material, Y-**thc**-MOF-2-f shows very limited uptake of N$_2$ at 77 K or EtOH at 298 K and no breathing phenomena (Figures S44, and S47). The absence of a flexible behavior during EtOH sorption contrasts with the parent Y-**thc**-MOF-2 and clearly demonstrates the crucial role of the coordinated 2-FBA ligand on the observed vapor dynamic behavior of the Y-**thc**-MOF-2. Accordingly, in Y-**thc**-MOF-2, the increased energetics associated with the highly deformed 2-FBA ligand, result in an

Figure 6. Vapor sorption isotherms of Y-**teb**-MOF-1 recorded at 298 K up to saturation pressure. Desorption branches are omitted for clarity.

increased energetic state of the framework that apparently requires less adsorption energy to form the open phase. In their absence, Y-**thc**-MOF-2-f in its closed form is energetically more stable to the extent that the provided vapor adsorption energy is not sufficient to trigger the phase transition towards the open structure.

It is noted that the reported formate-exchanged Y-**thc**-MOF-1 also lost its gas sorption dynamic properties, however EtOH adsorption experiments at 298 K did reveal the transition from the closed to the open phase[8] in marked contrast to Y-**thc**-MOF-2-f. Therefore, in the latter case, it is evident that additional factors are involved that control the dynamic response of the framework during vapor sorption. These factors can be found in the nature of the bridging ligand, where the presence of the pyridine-like central ring in Y-**thc**-MOF-2-f result in an increased conjugation with the adjacent benzoate groups, making their relative rotation from the closed to the open form, energetically more demanding. Apparently, EtOH adsorption at 298 K does not provide the necessary energy in the closed form of Y-**thc**-MOF-2-f to break the conjugation, resulting in a non-flexible behavior.

Regarding Y-**teb**-MOF-1-f, the absence of 2-FBA appears to be important for its flexible behavior. Prior to gas/vapor sorption measurements, the reversible flexible nature of Y-**teb**-MOF-1-f is confirmed by PXRD in both the as-made DMF-containing solid as well as in the EtOH-exchanged analogue (Figures S38 and S39). The N_2 sorption at 77 K reveals a significantly lower uptake (119.1 $cm^3 g^{-1}$ at 0.99 p/p_0) resulting in a total pore volume of 0.18 $cm^3 g^{-1}$, while no breathing steps are observed (Figure S48). Again, this behavior can be understood on the basis of an energetically more stable Y-**teb**-MOF-1-f, due to the absence of deformed 2-FBA ligands, where the provided gas adsorption energy is not adequate to open the framework. Preliminary vapor sorption experiments using EtOH, demonstrate a significant modification of the flexible properties (Figure S49). In particular, the corresponding adsorption isotherm recorded at 298 K shows an almost linear increase in uptake up to ~0.7 p/p_0 where thereafter, a more pronounced adsorption is observed, reaching an uptake of 114.8 $cm^3 g^{-1}$ at 0.99 p/p_0, close to the calculated value of the open phase (Figure S49). These results show that while the structure of Y-**teb**-MOF-1-f opens upon EtOH adsorption, the associated mechanism is different compared to Y-**teb**-MOF-1-f, showing a more continuous opening process. The absence of the low relative pressure sharp increase in EtOH uptake observed in Y-**teb**-MOF-1 (Figure 6), is consistent with the proposition that the removal of the coordinated 2-FBA ligand results in an energetically more stable closed phase that is more difficult to open upon EtOH adsorption.

Conclusions

This work unveils the unique opportunities offered in flexible RE-based MOFs, demonstrating that it is possible to use reticular chemistry to construct materials with distinct and controlled dynamic sorption properties. Following the impor-

tant discovery of the continuous breathing RE-**thc**-MOF-1 materials, by changing only one atom on the organic ligand used to construct the framework, the new isostructural analogue Y-**thc**-MOF-2 shows very different gas and vapor sorption properties. In particular, replacing benzene as the central aromatic ring of the ligand with a pyridine, results in a non-responsive closed structure upon gas sorption at cryogenic conditions. Strongly supported by SCXRD analysis, this significant change in gas-sorption framework flexibility is attributed to the particular nitrogen-based ligand conformation, where the increased conjugation between adjacent aromatic rings in the closed form of Y-**thc**-MOF-2 hinders the opening of the framework. Vapor sorption experiments also indicate that the transition from the closed to the open phase is more demanding in Y-**thc**-MOF-2 as compared to Y-**thc**-MOF-1, consistent with the gas-sorption data.

Further functionalization of the all-carbon ligand with methyl groups, to increase steric hindrance, afforded a novel series of flexible RE-based MOFs, RE-**teb**-MOF-1, with very similar layered structure as in RE-**thc**-MOF-x (x: 1, 2). Remarkably, extensive sorption studies of Y-**teb**-MOF-1 revealed continuous breathing properties coupled with trapping of various gases at their cryogenic conditions. The results indicate that the flexible dynamics of Y-**teb**-MOF-1 are associated with higher energetics compared to Y-**thc**-MOF-1. Extensive vapor sorption studies revealed a highly responsive behavior showing an S-type isotherm in all cases, with higher affinity for polar vapors such as EtOH and acetonitrile.

We have also gained further insight into the important factors that control the flexibility and sorption properties in these materials, by focusing on the particular role of the 2-FBA ligand coordinated on the Y_6-clusters. Replacement of these ligands with the smaller formate anions results in materials with very different flexible behavior upon gas and vapor sorption. The formate-exchanged solids are therefore considered as new variants of these families with distinct properties. These results demonstrate that, along with the linker functionalization, 2-FBA ligands play a critical cooperative role towards the eventual sorption properties of these RE-MOFs, including their ability to trap gas molecules.

Careful structural design with subtle changes can indeed induce remarkable and unprecedented modification in the responsive properties and help to better understand the associated structure-property relationship. To this end, our work provides important findings and open new directions towards a rational design of these important MOFs with great potential for advanced applications.

Experimental Section

General information: All chemicals were purchased commercially and were used without further purification. A detailed procedure for the synthesis of ligands H$_4$**L**$_1$ and H$_4$**L**$_2$, along with analytical data, can be found in the Supporting Information (pages S5-S9).

General synthetic procedure for the RE-thc-MOF-2 materials: RE-(NO$_3$)$_3$·xH$_2$O (0.045 mmol, x = 5 for Dy, Er or 6 for Y, Sm, Eu, Tb, Ho), 2-fluorobenzoic acid (1.43 mmol), H$_2$O (0.75 ml) and H$_4$**L**$_1$

Chemistry–A European Journal

Research Article
doi.org/10.1002/chem.202302709

Chemistry
Europe
European Chemical
Societies Publishing

(0.009 mmol) were added to a 1.45 ml solution of DMF, which was then placed in a 20 ml glass scintillation vial. The vial was sealed and placed in an isothermal oven at 120 °C for 24 hours. During this period yellow, prism-shaped crystals were formed. A detailed procedure for the synthesis of each MOF can be found in the Supporting Information (pages S11-S12).

General synthetic procedure for the RE-teb-MOF-1 materials: $RE(NO_3)_3 \cdot xH_2O$ (0.032 mmol, $x = 5$ for Er or 6 for Y, Eu), 2-fluorobenzoic acid (1.43 mmol), H_2O (0.75 ml) and H_4L_2 (0.00765 mmol) were added to a 2.72 ml solution of DMF, which was then placed in a 20 ml glass scintillation vial. The vial was sealed and placed in an isothermal oven at 120 °C for 24 hours. During this period colorless, prism-shaped crystals were formed. A detailed procedure for the synthesis of each MOF can be found in the Supporting Information (page S12).

Post-synthetic exchange of 2-fluorobenzoate with formate: To exchange the coordinated 2-FBA anions with formates the following procedure was performed: 20 mg of as-made Y-**thc**-MOF-2 or Y-**teb**-MOF-1 were immersed in a solution containing 5.2 ml of DMF and 0.2 mL of HCOOH (95%). The mixture was heated overnight at 100 °C. After cooling down, the crystalline solid was copiously washed with fresh DMF and was then stored in DMF. The complete removal of 2-FBA was confirmed by ^1H and ^{19}F NMR in an acid-digested sample (see Figures S57–S58, S62, S67 and S71).

NMR spectroscopy: ^1H and ^{19}F NMR spectra were recorded on a 500 MHz Bruker spectrometer. Chemical shifts are quoted in parts per million (ppm). **Powder X-Ray Diffraction (PXRD)**: PXRD patterns were collected using a Panalytical X'pert Pro MPD System Cu K_α ($\lambda = 1.5418$ Å) radiation operating at 45 kV and 40 mA. A typical scan rate was 1.5 sec/step with a step size of 0.02 deg. Calculated PXRD patterns from the corresponding single-crystal data were obtained using Mercury 3.8.[41] **Single Crystal X-ray Diffraction (SCXRD)**: SCXRD data were collected on a Bruker D8 Venture diffractometer equipped with a Cu Incoatec microfocus IμS 3.0 source, a Photon II detector operating in shutterless mode and a cryostream 800 system (Oxford Cryosystems) for temperature regulation. All structures were determined using OLEX2,[42] solved using SHELXT[43–44] and refined with SHELXL-2014.[45] More details can be found in the Supporting Information (pages S2–S4). Crystal data and structure refinement parameters for all reported structures are given in Tables S3-S15. **Deposition Number(s)** 2283269-2283272, 2283289-2283297 contain(s) the supplementary crystallographic data for this paper. These data are provided free of charge by the joint Cambridge Crystallographic Data Centre and Fachinformationszentrum Karlsruhe Access Structures service. **Scanning electron microscope (SEM)**: Images were obtained using a JEOL JSM-6390LV microscope equipped with the Oxford EDS detector. **Gas sorption measurements**. Low pressure N_2, Ar, CO_2 and CH_4 gas sorption measurements were carried at different temperatures up to 1 bar using a Quantachrome Autosorb-iQ2 instrument equipped with a cryocooler system capable of temperature control from 20 to 320 K. A detailed sample activation procedure can be found in the Supporting Information (page S4). **Vapor sorption measurements**. Vapor sorption isotherms (H_2O, EtOH, CH_3CN, C_6H_6, C_6H_{12}) were recorded at 298 K up to 1 bar, using a BELSORP-maxII instrument from Microtrac MRB, equipped with a detachable thermostatic bath for accurate measurements. Details on sample activation can be found in the Supporting Information (pages S4-S5). For comparison purposes, all isotherms are presented as the amount adsorbed as a function of the relative pressure, p/p_0, where p_0 is the saturation pressure of the vapor at the measurement temperature.

Supporting Information

The authors have cited additional references within the Supporting Information.[46–49]

Conflict of Interests

The authors declare no conflict of interest.

Data Availability Statement

The data that support the findings of this study are available in the supplementary material of this article.

[1] M. Bonneau, C. Lavenn, J. J. Zheng, A. Legrand, T. Ogawa, K. Sugimoto, F. X. Coudert, R. Reau, S. Sakaki, K. I. Otake, S. Kitagawa, *Nat. Chem.* **2022**, *14*, 816–822.

[2] S. Ehrling, E. M. Reynolds, V. Bon, I. Senkovska, T. E. Gorelik, J. D. Evans, M. Rauche, M. Mendt, M. S. Weiss, A. Poppl, E. Brunner, U. Kaiser, A. L. Goodwin, S. Kaskel, *Nat. Chem.* **2021**, *13*, 568–574.

[3] J. D. Evans, V. Bon, I. Senkovska, H. C. Lee, S. Kaskel, *Nat. Commun.* **2020**, *11*, 2690.

[4] E. Loukopoulos, G. K. Angeli, K. Kouvidis, C. Tsangarakis, P. N. Trikalitis, *ACS Appl. Mater. Interfaces* **2022**, *14*, 22242–22251.

[5] F. M. Amombo Noa, E. S. Grape, M. Ahlen, W. E. Reinholdsson, C. R. Gob, F. X. Coudert, O. Cheung, A. K. Inge, L. Ohrstrom, *J. Am. Chem. Soc.* **2022**, *144*, 8725–8733.

[6] R. Pallach, J. Keupp, K. Terlinden, L. Frentzel-Beyme, M. Kloss, A. Machalica, J. Kotschy, S. K. Vasa, P. A. Chater, C. Sternemann, M. T. Wharmby, R. Linser, R. Schmid, S. Henke, *Nat. Commun.* **2021**, *12*, 4097.

[7] S. Krause, N. Hosono, S. Kitagawa, *Angew. Chem. Int. Ed.* **2020**, *59*, 15325–15341.

[8] G. K. Angeli, E. Loukopoulos, K. Kouvidis, A. Bosveli, C. Tsangarakis, E. Tylianakis, G. Froudakis, P. N. Trikalitis, *J. Am. Chem. Soc.* **2021**, *143*, 10250–10260.

[9] Q. Dong, X. Zhang, S. Liu, R. B. Lin, Y. Guo, Y. Ma, A. Yonezu, R. Krishna, G. Liu, J. Duan, R. Matsuda, W. Jin, B. Chen, *Angew. Chem. Int. Ed.* **2020**, *59*, 22756–22762.

[10] R. B. Lin, L. Li, H. Wu, H. Arman, B. Li, R. G. Lin, W. Zhou, B. Chen, *J. Am. Chem. Soc.* **2017**, *139*, 8022–8028.

[11] M. K. Taylor, T. Runcevski, J. Oktawiec, J. E. Bachman, R. L. Siegelman, H. Jiang, J. A. Mason, J. D. Tarver, J. R. Long, *J. Am. Chem. Soc.* **2018**, *140*, 10324–10331.

[12] F. Walenszus, J. D. Evans, V. Bon, F. Schwotzer, I. Senkovska, S. Kaskel, *Chem. Mater.* **2021**, *33*, 7964–7971.

[13] J. H. Wang, M. Li, D. Li, *Chem. Sci.* **2013**, *4*, 1793–1801.

Chemistry–A European Journal

Research Article
doi.org/10.1002/chem.202302709

Chemistry Europe
European Chemical
Societies Publishing

[14] Z. Q. Yao, J. Xu, B. Zou, Z. Hu, K. Wang, Y. J. Yuan, Y. P. Chen, R. Feng, J. B. Xiong, J. Hao, X. H. Bu, *Angew. Chem. Int. Ed.* **2019**, *58*, 5614–5618.

[15] W. Cai, J. Wang, C. Chu, W. Chen, C. Wu, G. Liu, *Adv. Sci.* **2019**, *6*, 1801526.

[16] R. K. Das, A. Aijaz, M. K. Sharma, P. Lama, P. K. Bharadwaj, *Chem. Eur. J.* **2012**, *18*, 6866–6872.

[17] S. Yuan, L. Zou, H. Li, Y. P. Chen, J. Qin, Q. Zhang, W. Lu, M. B. Hall, H. C. Zhou, *Angew. Chem. Int. Ed.* **2016**, *55*, 10776–10780.

[18] F. X. Coudert, *Chem. Mater.* **2015**, *27*, 1905–1916.

[19] J. H. Lee, S. Jeoung, Y. G. Chung, H. R. Moon, *Coord. Chem. Rev.* **2019**, *389*, 161–188.

[20] A. Schneemann, V. Bon, I. Schwedler, I. Senkovska, S. Kaskel, R. A. Fischer, *Chem. Soc. Rev.* **2014**, *43*, 6062–6096.

[21] Y. Li, Y. Wang, W. Fan, D. Sun, *Dalton Trans.* **2022**, *51*, 4608–4618.

[22] S. Biswas, T. Ahnfeldt, N. Stock, *Inorg. Chem.* **2011**, *50*, 9518–9526.

[23] S. Henke, A. Schneemann, A. Wutscher, R. A. Fischer, *J. Am. Chem. Soc.* **2012**, *134*, 9464–9474.

[24] A. B. Kanj, K. Muller, L. Heinke, *Macromol. Rapid Commun.* **2018**, *39*.

[25] K. Rortocki, F. Formalik, V. Bon, A. Krawczuk, P. Goszczycki, B. Kuchta, S. Kaskel, D. Matoga, *Chem. Mater.* **2022**, *34*, 3430–3439.

[26] I. Senkovska, V. Bon, L. Abylgazina, M. Mendt, J. Berger, G. Kieslich, P. Petkov, J. Luiz Fiorio, J. O. Joswig, T. Heine, L. Schaper, C. Bachetzky, R. Schmid, R. A. Fischer, A. Poppl, E. Brunner, S. Kaskel, *Angew. Chem. Int. Ed.* **2023**, *62*, e202218076.

[27] X. L. Lv, L. Feng, L. H. Xie, T. He, W. Wu, K. Y. Wang, G. Si, B. Wang, J. R. Li, H. C. Zhou, *J. Am. Chem. Soc.* **2021**, *143*, 2784–2791.

[28] J. K. Schnobrich, O. Lebel, K. A. Cychosz, A. Dailly, A. G. Wong-Foy, A. J. Matzger, *J. Am. Chem. Soc.* **2010**, *132*, 13941–13948.

[29] Y. Wang, L. Feng, K. Zhang, K. Y. Wang, W. Fan, X. Wang, B. Guo, F. Dai, L. Zhang, D. Sun, H. C. Zhou, *Adv. Sci.* **2019**, *6*, 1901855.

[30] Y. Y. Zhu, J. M. Gu, X. Y. Yu, B. R. Zhang, G. H. Li, J. T. Li, Y. L. Liu, *Inorg. Chem. Front.* **2021**, *8*, 4990–4997.

[31] D. Alezi, A. M. Peedikakkal, L. J. Weselinski, V. Guillerm, Y. Belmabkhout, A. J. Cairns, Z. Chen, L. Wojtas, M. Eddaoudi, *J. Am. Chem. Soc.* **2015**, *137*, 5421–5430.

[32] G. K. Angeli, C. Sartsidou, S. Vlachaki, I. Spanopoulos, C. Tsangarakis, A. Kourtellaris, E. Klontzas, G. E. Froudakis, A. Tasiopoulos, P. N. Trikalitis, *ACS Appl. Mater. Interfaces* **2017**, *9*, 44560–44566.

[33] V. Guillerm, L. Weselinski, Y. Belmabkhout, A. J. Cairns, V. D'Elia, L. Wojtas, K. Adil, M. Eddaoudi, *Nat. Chem.* **2014**, *6*, 673–680.

[34] D. X. Xue, A. J. Cairns, Y. Belmabkhout, L. Wojtas, Y. Liu, M. H. Alkordi, M. Eddaoudi, *J. Am. Chem. Soc.* **2013**, *135*, 7660–7667.

[35] Z. Ajoyan, G. A. Mandl, P. R. Donnarumma, V. Quezada-Novoa, H. A. Bicalho, H. M. Titi, J. A. Capobianco, A. J. Howarth, *ACS Mater. Lett.* **2022**, *4*, 1025–1031.

[36] J. I. Deneff, L. E. S. Rohwer, K. S. Butler, N. R. Valdez, M. A. Rodriguez, T. S. Luk, D. F. Sava Gallis, *ACS Appl. Mater. Interfaces* **2022**, *14*, 3038–3047.

[37] J. P. Vizuet, M. L. Mortensen, A. L. Lewis, M. A. Wunch, H. R. Firouzi, G. T. McCandless, K. J. Balkus, Jr., *J. Am. Chem. Soc.* **2021**, *143*, 17995–18000.

[38] Z. R. Herm, B. M. Wiers, J. A. Mason, J. M. van Baten, M. R. Hudson, P. Zajdel, C. M. Brown, N. Masciocchi, R. Krishna, J. R. Long, *Science* **2013**, *340*, 960–964.

[39] H. Wang, X. Dong, J. Lin, S. J. Teat, S. Jensen, J. Cure, E. V. Alexandrov, Q. Xia, K. Tan, Q. Wang, D. H. Olson, D. M. Proserpio, Y. J. Chabal, T. Thonhauser, J. Sun, Y. Han, J. Li, *Nat. Commun.* **2018**, *9*, 1745.

[40] F. X. Coudert, M. Jeffroy, A. H. Fuchs, A. Boutin, C. Mellot-Draznieks, *J. Am. Chem. Soc.* **2008**, *130*, 14294–14302.

[41] C. F. Macrae, P. R. Edgington, P. McCabe, E. Pidcock, G. P. Shields, R. Taylor, M. Towler, J. van De Streek, *J. Appl. Crystallogr.* **2006**, *39*, 453–457.

[42] O. V. Dolomanov, A. J. Blake, N. R. Champness, M. Schroder, *J. Appl. Crystallogr.* **2003**, *36*, 1283–1284.

[43] G. M. Sheldrick, *Acta Crystallogr. Sect. A* **2008**, *64*, 112–122.

[44] G. M. Sheldrick, *Acta Crystallogr. Sect. A* **2015**, *71*, 3–8.

[45] G. M. Sheldrick, *Acta Crystallogr. Sect. C* **2015**, *71*, 3–8.

[46] G. W. V. Cave, C. L. Raston, *Chem. Commun.* **2000**, 2199–2200.

[47] A. L. Spek, *J. Appl. Crystallogr.* **2003**, *36*, 7–13.

[48] B. Wang, R. He, L. H. Xie, Z. J. Lin, X. Zhang, J. Wang, H. L. Huang, Z. J. Zhang, K. S. Schanze, J. Zhang, S. C. Xiang, B. L. Chen, *J. Am. Chem. Soc.* **2020**, *142*, 12478–12485.

[49] H. Xu, X. F. Liu, C. S. Cao, B. Zhao, P. Cheng, L. N. He, *Adv. Sci.* **2016**, *3*: 1600048.